ACS central science

http://pubs.acs.org/journal/acscii

Research Article

Thousand-fold increase in O_2 electroreduction rates with conductive MOFs

Ruperto G. Mariano, Oluwasegun J. Wahab,[‖] Joshua A. Rabinowitz,[‖] Julius Oppenheim, Tianyang Chen, Patrick R. Unwin,* and Mircea Dincă*

Cite This: *ACS Cent. Sci.* 2022, 8, 975−982

Read Online

ACCESS | Metrics & More | Article Recommendations | Supporting Information

ABSTRACT: Molecular materials must deliver high current densities to be competitive with traditional heterogeneous catalysts. Despite their high density of active sites, it has been unclear why the reported O_2 reduction reaction (ORR) activity of molecularly defined conductive metal−organic frameworks (MOFs) have been very low: ca. −1 mA cm^{-2}. Here, we use a combination of gas diffusion electrolyses and nanoelectrochemical measurements to lift multiscale O_2 transport limitations and show that the intrinsic electrocatalytic ORR activity of a model 2D conductive MOF, $Ni_3(HITP)_2$, has been underestimated by at least 3 orders of magnitude. When it is supported on a gas diffusion electrode (GDE), $Ni_3(HITP)_2$ can deliver ORR activities >−150 mA cm^{-2} and gravimetric H_2O_2 electrosynthesis rates exceeding or on par with those of prior heterogeneous electrocatalysts. Enforcing the fastest accessible mass transport rates using scanning electrochemical cell microscopy revealed that $Ni_3(HITP)_2$ is capable of ORR current densities exceeding −1200 mA cm^{-2} and at least another 130-fold higher ORR mass activity than has been observed in GDEs. Our results directly implicate precise control over multiscale mass transport to achieve high-current-density electrocatalysis in molecular materials.

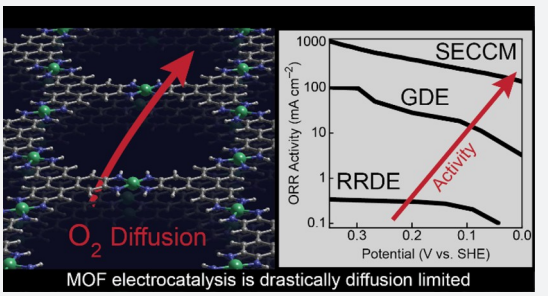

INTRODUCTION

Achieving synthetic molecular control over electrocatalytic materials is a longstanding challenge in electrocatalysis. Molecular materials need to deliver high current densities to be competitive with heterogeneous electrocatalysts, but this is rare.[1] Electrically conductive metal−organic frameworks (MOFs) offer a way to bridge this gap, as they are molecularly defined and are both intrinsically porous and conductive.[2] They are fundamentally distinct from electrocatalysts made from sacrificial MOF precursors (such as single-atom catalysts accessed via thermolysis or electrolytic degradation of MOFs), because they retain their molecular definition.[3,4,13,14,5−12] As such, the structure space available to conductive MOFs renders them an ideal platform to tune the atomic structure for performance. We and others have previously shown that a family of 2D MOFs with the general formula $M_3(HITP)_2$ (HITP = 2,3,6,7,10,11-hexaiminotriphenylene, M = Co, Cu, Ni) (Figure 1A) are active for the O_2 electroreduction reaction (ORR), a transformation central to H_2O_2 electrosynthesis, metal/air batteries, and fuel cells.[4,15,16] These and other conductive MOFs typically exhibit intrinsic surface areas (~300−900 m^2 g^{-1}) at least 10 times larger than that of dense metallic nanoparticles and conductivities comparable to that of graphite, yet their geometric current densities for ORR rarely exceed −1 mA cm^{-2}, implying a surprisingly low intrinsic electrocatalytic activity.[2,4,5,15,17−19]

The performance of ORR electrocatalysts is most commonly measured using rotating ring disk electrodes (RRDEs) immersed in an electrolyte within two-compartment "H-cells".[4,20,21] During ORR catalysis in an H-cell, a region of depleted O_2 concentration (the concentration boundary, or diffusion layer) is formed adjacent to the catalyst layer (Figure 1B), because O_2 is reduced to H_2O_2 or H_2O at the electrode/electrolyte interface. In combination with the low saturation concentration of O_2 in water (~1 mM at 1 bar of O_2 and 298 K), O_2 must diffuse over distances of ca. 100 μm from the bulk electrolyte in order to reach the electrode/electrolyte interface.[22] Concentration gradients are further exacerbated in porous electrodes, where diffusion within the porous layer can be severely restricted;[23,24] the resulting transport resistance depresses the mass activity of the electrocatalyst and leads to underutilization of the active sites.

Under these circumstances, it is unclear whether the −1 mA cm^{-2} limit arises from mass transport limitations or in fact reflects intrinsically slow ORR kinetics with molecular materials. To probe the fundamental limitations of ORR catalysis with

Received: April 28, 2022
Published: July 1, 2022

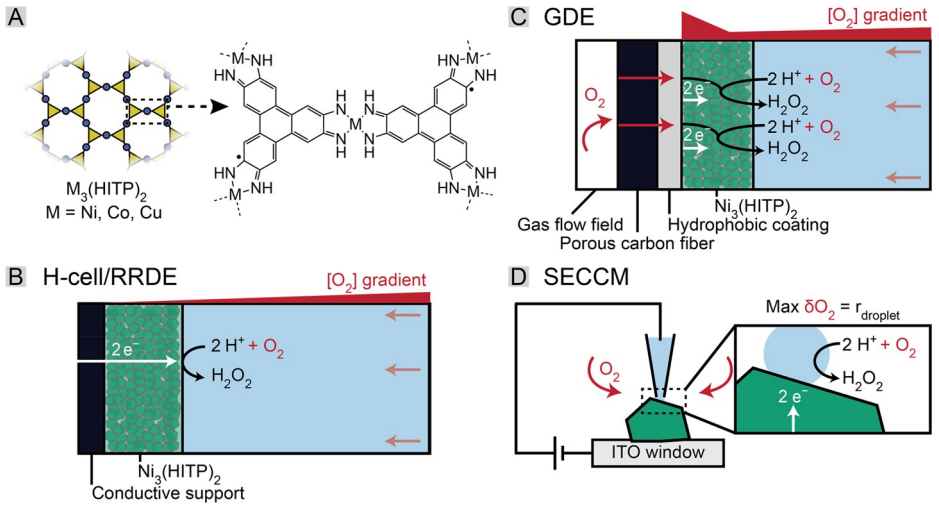

Figure 1. Controlling mass transport during ORR electrocatalysis with conductive MOFs: (A) atomic structure and connectivity of $M_3(HITP)_2$; (B) schematic of transport gradients during ORR catalysis in a conventional electrochemical H-cell using RRDEs; (C) schematic of transport dynamics in a GDE combined with flow fields; (D) mass transport of O_2 across a nanodroplet in SECCM.

MOFs and potentially unlock a much higher intrinsic activity, we pursued a campaign to lift mass transport limitations by integrating $Ni_3(HITP)_2$ with gas diffusion electrodes (GDEs) and by leveraging the rapid transport environment afforded by scanning electrochemical cell microscopy (SECCM).

Here, we show that conductive MOFs enable geometric ORR current densities greater than -150 mA cm^{-2} if the mass transport of O_2 is carefully controlled. When it is supported on a GDE (Figure 1C), $Ni_3(HITP)_2$ exhibits ORR activity and H_2O_2 electrosynthesis rates >100-fold higher and >740-fold higher, respectively, than in an H-cell. At low mass loadings in a GDE, the gravimetric rates of H_2O_2 electrosynthesis using $Ni_3(HITP)_2$ rival those of the highest rates reported for state of the art heterogeneous electrocatalysts. Together with efficient O_2 mass transport, metal ion substitution revealed that the intrinsic porosity and conductivity of $M_3(HITP)_2$ are the major drivers of activity during ORR catalysis. By enforcing the fastest accessible mass transport rates using SECCM (Figure 1D), we find that $Ni_3(HITP)_2$ is capable of at least another 130-fold higher mass activity than has been observed in GDEs. Our results directly implicate precise control over mass transport to achieve high-current-density electrocatalysis in molecularly defined, conductive MOFs.

RESULTS AND DISCUSSION

Due to its high conductivity, intrinsic porosity, and established activity for the ORR, we prepared $Ni_3(HITP)_2$, an archetypal 2D conductive MOF, to understand mass transport effects on ORR catalysis.[19] Powder X-ray diffraction (PXRD) patterns (Figure S1) and X-ray photoelectron spectra (XPS; Figure S2) were consistent with literature precedent and indicated the formation of a monophasic and highly crystalline 2D framework.[19,25] N_2 adsorption measurements of $Ni_3(HITP)_2$ (Figure S3) at 77 K after activation at 373 K under dynamic vacuum revealed a high Brunauer–Emmett–Teller (BET) surface area of 802 ± 0.8 m^2 g^{-1}. SEM imaging (Figure S4) indicated that the $Ni_3(HITP)_2$ powders were composed of crystallites measuring 50–200 nm agglomerated into 1 μm wide clusters.

We drop-cast a suspension of as-synthesized $Ni_3(HITP)_2$ particles sonicated with Nafion (to act as a binder; see the Supporting Information and Figure S5) onto glassy-carbon electrodes (GCEs) for a total mass loading of 0.4 mg cm^{-2} of $Ni_3(HITP)_2$. We then evaluated the performance of the $Ni_3(HITP)_2$-loaded GCEs for the ORR in a two-compartment H-cell combined with a RRDE setup (Figure 2B). We measured cyclic voltammograms (CVs) in O_2 and N_2, using 1.0 M sodium chloride electrolyte buffered with 0.3 M sodium phosphate (NaP_i) at pH 7. Polarization from +0.21 to -0.29 V versus the standard hydrogen electrode (SHE, to which all potentials are referenced), indicated that $Ni_3(HITP)_2$ exhibited less than -1 mA cm^{-2} O_2 electroreduction activity. The onset of catalytic activity was observed at -0.05 V, and a plateau in the CV (around -0.6 mA cm^{-2}) was observed beginning at -0.2 V (Figure 2B, inset). Polarization to more negative potentials or an increase in the rotation rate did not significantly increase the current density for O_2 reduction (j_{ORR}; Figure S6A,B). We quantified the partial current density for H_2O_2 synthesis ($j_{H_2O_2}$) under potentiostatic conditions while applying an oxidizing potential of 0.91 V at the Pt ring to simultaneously detect H_2O_2.[15] (Figure 2C,D). The Faradaic efficiency (FE) for H_2O_2 peaked at 60% (-0.121 mA cm^{-2}) at 0.09 V and decreased upon application of more cathodic potentials, dropping to 21% (-0.085 mA cm^{-2}) at -0.54 V (Figure S6C). The small limiting current values ($j_{ORR} = -0.4$ mA cm^{-2}) are less than expected from the Koutecky–Levich equation ($j_d \approx -2.5$ mA cm^{-2} at 1500 rpm for the $2e^-$ process), indicative of slow O_2 mass transport not only from the bulk solution to the $Ni_3(HITP)_2$ catalyst layer but also within the immersed $Ni_3(HITP)_2$/Nafion catalyst layer.[20]

To investigate whether the ORR activity of $Ni_3(HITP)_2$ would improve under a rapid bulk mass transport regime, we drop-casted $Ni_3(HITP)_2$ particles onto GDEs, at the same mass loading of 0.4 mg cm^{-2} (SEM imaging in Figure S7 and S8). Composed of a carbon fiber support and a hydrophobic microporous conductive coating, GDEs enhance gas mass transport by providing a gas flow pathway unimpeded by electrolyte through the back of the electrode (Figure 1C). $Ni_3(HITP)_2$ GDEs were interfaced into a custom-built gas diffusion flow electrolyzer (Figure 2A, detailed in the Supporting Information)[26−29] with a microfluidic pocket that limits the contact area (~0.8 cm^2) between the MOF-loaded GDE and electrolyte (Figure 2A). The $Ni_3(HITP)_2$ GDE was compressed

https://doi.org/10.1021/acscentsci.2c00509
ACS Cent. Sci. 2022, 8, 975−982

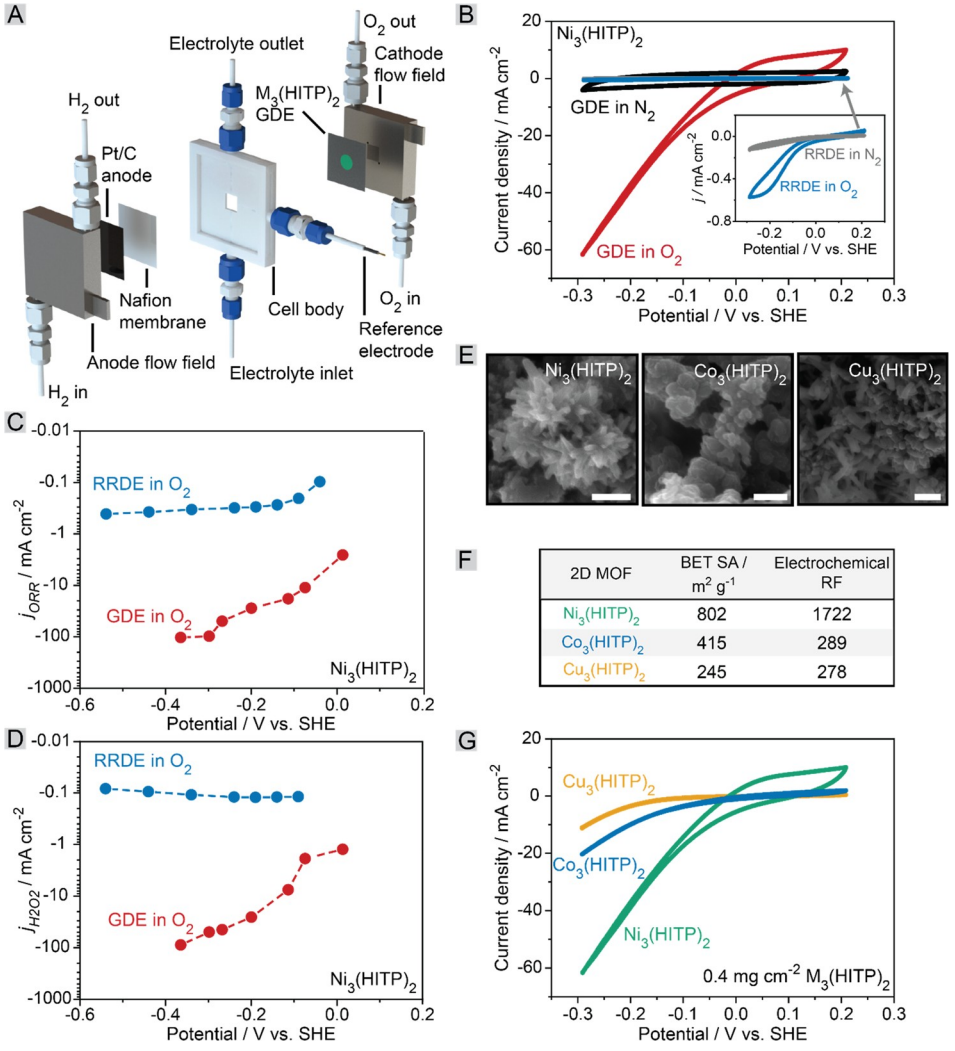

2D MOF	BET SA / $m^2\ g^{-1}$	Electrochemical RF
$Ni_3(HITP)_2$	802	1722
$Co_3(HITP)_2$	415	289
$Cu_3(HITP)_2$	245	278

Figure 2. Polarization of $M_3(HITP)_2$ in an H-cell and using a GDE flow electrolyzer. All current densities reported are normalized to the geometric surface area. (A) Schematic of the gas diffusion flow electrolysis cell used in this study. (B) Cyclic voltammograms of 0.4 mg cm^{-2} $Ni_3(HITP)_2$ GDEs in 1 M NaCl, 0.3 M sodium phosphate (NaP_i) electrolyte at pH 7. Inset CVs show RRDE data at the same 0.4 mg cm^{-2} mass loading, but where the current scale is much smaller. Scan rate: 50 mV s^{-1}. The RRDE was rotated at 1000 rpm. Potentials vs SHE reported in (B) are not corrected for the system *iR* drop. (C) Geometric current densities for O_2 reduction during potentiostatic polarization for both the RRDE and GDE electrolyses. The RRDE was rotated at 1500 rpm. (D) Partial current densities for H_2O_2 synthesis during potentiostatic polarization for both the RRDE and GDE electrolyses. The RRDE was rotated at 1500 rpm. (E) SEM images of $M_3(HITP)_2$. Scale bar: 200 nm. (F) BET surface area derived from N_2 adsorption measurements and electrochemical roughness factors (RF) represented as multiples of geometric surface area, calculated from CVs obtained in N_2. (G) CVs of the three isoreticular $M_3(HITP)_2$ GDEs in O_2. Scan rate: 50 mV s^{-1}.

against a conductive, interdigitated flow field that rapidly transports O_2 to the $Ni_3(HITP)_2$/electrolyte interface. Electrolyte flowed through the cell and into a collection vial, enabling quantification of electrogenerated H_2O_2. Enhancing O_2 transport to the $Ni_3(HITP)_2$/electrolyte interface led to orders of magnitude higher ORR current densities using $Ni_3(HITP)_2$ GDEs. Across the same potential range as was used with RRDEs, CVs of a $Ni_3(HITP)_2$ GDE indicated that the geometric j_{ORR} was ca. 1−2 orders of magnitude larger with the GDE relative to the RRDE (Figure 2B). At −0.29 V, whereas $Ni_3(HITP)_2$ exhibited a j_{ORR} value of only −0.6 mA cm^{-2} on the RRDE, its activity on the GDE was −62 mA cm^{-2}. Control experiments of both the GDE support under an O_2 atmosphere (Figure S9) and the $Ni_3(HITP)_2$ GDE under an N_2 atmosphere (Figure 2B) indicated that essentially all of the observed current could be attributed to ORR catalysis (i.e., no H_2 evolution) occurring at the $Ni_3(HITP)_2$ sites. These data indicate that $Ni_3(HITP)_2$ was starved of O_2 during polarization in the H-cell, which led to a vast underestimation of its intrinsic electrocatalytic performance.

We evaluated the ORR performance of the $Ni_3(HITP)_2$ GDEs by measuring the current during step-potential polarization (Figure 2C). Unlike the case in the H-cell, the geometric j_{ORR} value using the GDE increased monotonically with the applied potential in a broader range, reaching a maximum current density of −103 mA cm^{-2} at −0.36 V, an approximately 310-fold improvement in j_{ORR} relative to those measured in the RRDE/H-cell. Similarly, the $j_{H_2O_2}$ value using the $Ni_3(HITP)_2$ GDE increased as a function of applied potential from −1.2 mA cm^{-2} at 0.01 V to a maximum current density of −88.5 mA cm^{-2} (or 85% FE for H_2O_2) at −0.36 V, a 740-fold improvement over the maximum $j_{H_2O_2}$ value measured using the RRDE/H-cell at the same mass loading (Figure 2D). With 0.2 mL min^{-1} of electrolyte flowing through the cell, we measured a 108 mM

https://doi.org/10.1021/acscentsci.2c00509
ACS Cent. Sci. 2022, 8, 975−982

(~3270 ppm) H_2O_2 product stream at −0.36 V. These high ORR current densities corresponded to a mass activity of 259 A g^{-1} at −0.36 V, which is competitive with state of the art, H_2O_2-producing heterogeneous electrocatalysts in a neutral electrolyte.[30] PXRD patterns and XPS spectra obtained immediately after polarization indicated that $Ni_3(HITP)_2$ retained its crystallinity, and we found no evidence for the formation of metallic Ni from reduction of framework Ni^{2+} (Figures S10 and S11). As H_2O_2 concentrations were likely even higher within the $Ni_3(HITP)_2$ pores, these data indicate that $Ni_3(HITP)_2$ is stable to high local concentrations of electrogenerated H_2O_2.

Supporting conductive MOFs on GDEs is a general strategy that allowed us to probe the effect of metal ion substitution in $M_3(HITP)_2$ under a high O_2 flux. We integrated two additional, isostructural HITP-based frameworks, namely $Cu_3(HITP)_2$ and $Co_3(HITP)_2$ with GDEs (Figure 2E−G; characterization in Text 1 in the Supporting Information and Figures S12−S17), to evaluate their ORR activity under high-mass-transport conditions.[25] Polarization in O_2 revealed that the total j_{ORR} and $j_{H_2O_2}$ values both depend on the identity of the MOF and vary in the order Ni > Co > Cu (Figure 2G). This reflected the trend in electrochemical surface area (ECSA, a composite value of intrinsic surface area and conductivity) among the three MOFs (Ni > Co > Cu; Figure 2F and Figure S18). $Ni_3(HITP)_2$ exhibits more than 6-fold higher ECSAs in comparison to the Cu or Co analogues, characteristic of its high conductivity and porosity. On a mass activity basis, $Ni_3(HITP)_2$ exhibits the highest activity at the lowest driving forces (Figure S17A). These data provided a simple model to rationalize the observed j_{ORR} value: $Ni_3(HITP)_2$ is the most active of the three $M_3(HITP)_2$ because it possesses an intrinsically higher ECSA and therefore a higher density of active sites. Given that crystallinity generally engenders high conductivity and surface area in conductive MOFs, and noting that as-synthesized $Ni_3(HITP)_2$ is intrinsically more crystalline than either $Co_3(HITP)_2$ or $Cu_3(HITP)_2$ (cf. Figures S1 and S12), these results suggest that high conductivity, porosity, and crystallinity are the keys to unlocking high rates of ORR catalysis in MOFs.[2]

Motivated by the apparent dependence of j_{ORR} on $M_3(HITP)_2$ ECSA in the GDE and because maximizing j_{ORR} is technologically desirable, we sought to understand how much of the ECSA in $Ni_3(HITP)_2$ could be productively recruited for catalysis. To this end, we varied the $Ni_3(HITP)_2$ mass loading from 0.1 to 0.8 mg cm^{-2} (Figure 3; chronoamperograms are given in Figure S20). The geometric j_{ORR} value generally increased with higher catalyst loading (Figure 3A). For instance, at −0.36 V, the geometric j_{ORR} value at 0.4 mg cm^{-2} was ~2-fold higher than that at 0.1 mg cm^{-2}. CVs in N_2 showed that the ECSA also increased with increased mass loading (Figure S21 and Table S1). These mass-dependent increases in ECSA correlate with the increase in j_{ORR} and indicate a larger number of active sites available for ORR catalysis. Additionally, higher values of $j_{H_2O_2}$ are correlated with higher mass loadings of up to 0.4 mg cm^{-2} (Figure 3B). At −0.36 V, $j_{H_2O_2}$ increased ~3.3-fold as the mass loading increased from 0.1 to 0.4 mg cm^{-2}. We did not observe a systematic correlation between mass loading and FE (Figure S22A), suggesting that $2e^-$ reduction of H_2O_2 to H_2O, or framework-catalyzed decomposition of H_2O_2 to O_2, does not accelerate with higher mass loadings under the conditions employed here.

At a high overpotential, the mass activity decreases as the catalyst loading increases (Figure 3C and Figure S22B), with the lowest mass loading of 0.1 mg cm^{-2} being responsible for the highest mass activity of 553 A g^{-1} at the most cathodic applied potential. At the highest applied potentials, the rate of H_2O_2 production using the 0.1 mg cm^{-2} electrode is equivalent to a gravimetric rate of 6570 mol H_2O_2 kg_{MOF}^{-1} h^{-1}, better than or competitive with the highest activities reported among state of the art H_2O_2-evolving electrocatalysts.[30−32]

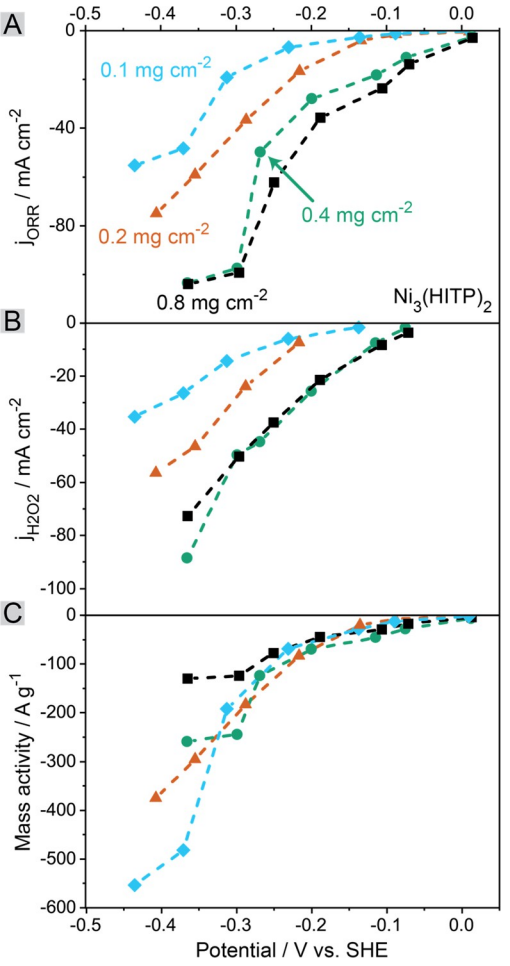

Figure 3. ORR activity limits in $Ni_3(HITP)_2$ GDEs. (A) Geometric current densities for the ORR during potentiostatic polarization with different catalyst mass loadings: (◆) 0.1 mg cm^{-2}; (▲) 0.2 mg cm^{-2}; (●) 0.4 mg cm^{-2}; (■) 0.8 mg cm^{-2}. (B) Partial current densities for H_2O_2 synthesis during potentiostatic polarization. (C) Comparison of total ORR mass activities of the four different mass loadings.

Although low $Ni_3(HITP)_2$ mass loadings yield the highest mass activities (Figure 3C), they also exhibit the lowest geometric j_{ORR} and $j_{H_2O_2}$ values (Figure 3A,B). This an important dilemma to address, because it implies that much of the ECSA in $Ni_3(HITP)_2$ GDEs remained underutilized at high mass loading. Indeed, an apparent plateau in the geometric j_{ORR} value (ca. −110 mA cm^{-2}) is observed for GDEs with 0.4 and 0.8 mg cm^{-2} of $Ni_3(HITP)_2$ at a high driving force. The contrast between the 0.8 and 0.4 mg cm^{-2} electrodes is small: doubling the mass loading provides only marginal improvements at low overpotentials and essentially identical activity at high overpotentials. Moreover, the $j_{H_2O_2}$ value for the 0.8 mg cm^{-2} electrode is only ~80% of that for the 0.4 mg cm^{-2} electrode (Figure 3B). If the mass activity of the 0.8 mg cm^{-2} electrode were identical with that of the 0.1 mg cm^{-2} electrode (481 A g^{-1}

https://doi.org/10.1021/acscentsci.2c00509
ACS Cent. Sci. 2022, 8, 975−982

at −0.36 V), the measured j_{ORR} value for the 0.8 mg cm^{-2} electrode should be >380 mA cm^{-2}, almost 4× larger than what we observe. In fact, mass activities across the four different mass loadings were relatively uniform at low overpotentials and diverged prominently only at high overpotentials (Figure 22B). This activity plateau limited the single-pass O_2 conversion rate to just 30% (Figure S22C).

High-resolution scanning electrochemical cell microscopy (SECCM; Figure 4A)[33−35] lent critical insight into the origin of

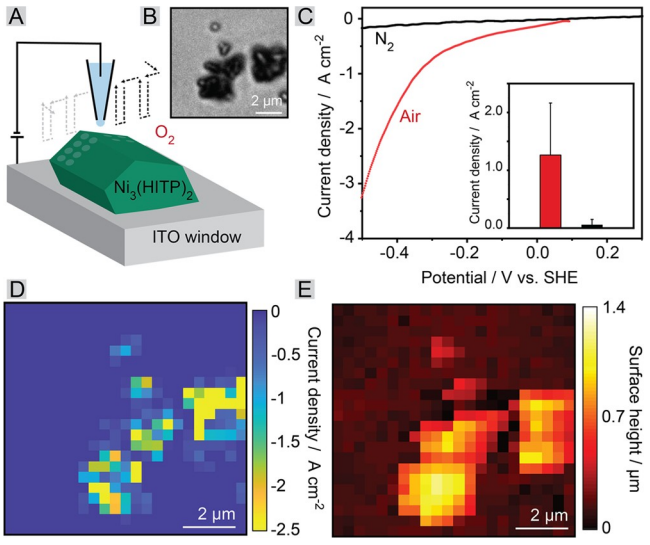

Figure 4. SECCM mapping of ORR activity on $Ni_3(HITP)_2$. (A) Schematic of the experimental geometry in SECCM using a single-barrel nanopipet. (B) Optical image of the $Ni_3(HITP)_2$ particles scanned using SECCM under air. (C) Single-pixel LSVs of $Ni_3(HITP)_2$ obtained under N_2 and air. Inset: average current densities at −0.36 V for $Ni_3(HITP)_2$ under N_2 and air. SECCM scans corresponding to those in N_2 are shown in Figure S24. (D) SECCM map of geometric current densities (defined as the current divided by the tip droplet area) measured on $Ni_3(HITP)_2$ at −0.36 V. (E) Corresponding topographic map of $Ni_3(HITP)_2$ derived from SECCM mapping.

the plateau in activity observed in our GDE studies (Figure S23 and the Supporting Information for experimental details). By confinement of the entirety of the electrode contact area to the footprint of a droplet at the end of a nanopipet, SECCM offers the fastest gas mass transport rates experimentally accessible for electrocatalysis: N_2 or O_2 can rapidly traverse the nanoscale droplet electrolyte and the porous $Ni_3(HITP)_2$ particles, with the maximum diffusion length of gaseous species to the catalyst surface being set by the droplet radius.[28,36] For example, a hemispherical droplet with a radius r_d = 25 nm has a sub-microsecond diffusion time, about 6 orders of magnitude higher than that in the RRDE studies. By confining electrocatalytic studies to a nanoscale droplet, SECCM provides a unique platform to measure the intrinsic electrochemical mass activity in the absence of extrinsic transport limitations.

Using a 50 nm diameter nanopipet filled with a solution of 30 mM NaP_i (pH 7) and 100 mM NaCl, we directly mapped the electrochemical activity of $Ni_3(HITP)_2$ particles under cathodic polarization under both N_2 and air (P_{O_2} = 0.2 bar) (Figure S24 and Figure 4, respectively).[37] The average current under N_2 at −0.36 V was negligible at ca. −1 pA, close to the noise limit of the conditions we employ here (Figure S24, Movie S1, histograms in Figure S29). Comparison of individual linear sweep voltammograms (LSVs) in N_2 versus those in air indicated that essentially all of the measured current in air arose from the ORR (Figure 4C). Importantly, control experiments probing the nanodroplet while it was in contact with $Ni_3(HITP)_2$ revealed that the droplet was stable while it was in contact with the MOF. Furthermore, the droplet contact areas were similar on both $Ni_3(HITP)_2$ and ITO, allowing us to estimate the maximum ECSA of $Ni_3(HITP)_2$ contacted during SECCM measurements. (Text 2 in the Supporting Information and Figures S26−S29).

In contrast, SECCM scans of $Ni_3(HITP)_2$ under air indicated high ORR activity across the MOF particle surface, with an average current of −25 pA at −0.36 V vs SHE (Figure 4B,C, Movie S2, and histograms in Figure S29B). Given a droplet radius of 25 nm, this current translates to a geometric j_{ORR} value of −1273 mA cm^{-2}, 38-fold greater than the highest current densities observed under air using the GDE (Figure S25). The larger current densities observed in SECCM versus the GDE or RRDE configurations are consistent with the short diffusion pathways enforced by the nanoscopic dimensions of SECCM.[28,35,38−51]

Using the SECCM and topography maps obtained under air, we calculated a lower-bound estimate of the intrinsic mass activity of $Ni_3(HITP)_2$, making a conservative assumption that all of the cylindrical mass of $Ni_3(HITP)_2$ under the droplet's 50 nm footprint is recruited for catalysis (Figure S30). Strikingly, these estimates yielded a lower-bound average mass activity of 11250 A g^{-1} at −0.36 V vs SHE, 136-fold higher than the highest mass activities measured with GDEs in air.

The rapid transport environment of SECCM revealed that $Ni_3(HITP)_2$ is even more active intrinsically than has been observed in the GDE, suggesting that even at low mass loadings some O_2 mass transport resistance persists in the agglomerated $Ni_3(HITP)_2$ GDE catalyst layer. At high $Ni_3(HITP)_2$ GDE mass loadings, much of the active material is immersed in a thick aqueous electrolyte layer through which O_2 mass transport is sluggish (Figure S31), with maximum diffusion lengths likely exceeding the thickness of the flooded GDE pores and $Ni_3(HITP)_2$ catalyst layer (>10 μm; see Figure S8).

Crucially, the high mass activities observed in SECCM mean that the activity plateau observed in the GDE was extrinsic to $Ni_3(HITP)_2$. Identifying slow micrometer-scale O_2 mass transport, rather than low intrinsic catalyst activity, as the origin of current density limitations observed in the GDE provides an impetus to improve the mass transport properties of the $Ni_3(HITP)_2$ GDE. As a simple proof of principle, we reformulated the catalyst ink to include 10 wt % of hydrophobic polytetrafluoroethylene (PTFE) powder that was intimately mixed with the $Ni_3(HITP)_2$ nanoparticles, reducing $Ni_3(HITP)_2$ particle agglomeration and providing continuous, hydrophobic channels through which O_2 could diffuse rapidly (Figures S31−S34 and Text 3 in the Supporting Information).[26,29]

The facility of O_2 transport across the hydrophobic PTFE domains led to substantial increases in ORR activity: a 0.8 mg cm^{-2} $Ni_3(HITP)_2$ GDE with 10 wt % added PTFE passed a total current density of −170 mA cm^{-2} at just −0.27 V (Figure S34A). By comparison, the previous best-performing PTFE-free 0.4 mg cm^{-2} $Ni_3(HITP)_2$ electrode reached a peak j_{ORR} value of −103 mA cm^{-2} while also requiring a 90 mV higher driving force of −0.36 V. This activity translated to a 60% higher total single-pass O_2 conversion rate of 48% at an O_2 flow rate of 1.5 mL min^{-1} (Figure S34F). With the addition of 10 wt % PTFE, the 0.8 mg

https://doi.org/10.1021/acscentsci.2c00509
ACS Cent. Sci. 2022, 8, 975−982

cm^{-2} electrode exhibits 70% greater mass activity than its PTFE-free analogue: 212 vs ∼124 A g^{-1} (Figure S34C). Incorporating PTFE into the catalyst ink increased the apparent mass-transport-limited current from −110 to −180 mA cm^{-2}, an increase of ∼60%. These large differences in activity demonstrate that enhancing O_2 mass transport in the $Ni_3(HITP)_2$ catalyst layer allows more of the $Ni_3(HITP)_2$'s ECSA to be recruited for productive catalysis. However, the mass activity of the 10% PTFE electrode with 0.8 mg cm^{-2} $Ni_3(HITP)_2$ remains more than a factor of 2 below the mass activity of the PTFE-free electrode with only 0.1 mg cm^{-2} $Ni_3(HITP)_2$ and >50-fold below those recorded in SECCM. Further improvements in the geometric j_{ORR} value in practical devices are gated not by the intrinsic activity of $Ni_3(HITP)_2$ but by the facility of O_2 mass transport. Identifying the multiscale transport bottlenecks that prevent MOFs from delivering high current densities motivates the broader exploration and deployment of these designer materials for a variety of electrocatalytic processes.

■ ASSOCIATED CONTENT

Supporting Information

The Supporting Information is available free of charge at . (PDF). The Supporting Information is available free of charge at https://pubs.acs.org/doi/10.1021/acscentsci.2c00509.

Experimental details, materials and electrochemical characterization, Texts 1−3, SECCM control experiments, mass activity estimation, and movie captions (PDF)

Spatially resolved electrochemical video of $Ni_3(HITP)_2$ under an N_2 atmosphere (AVI)

Spatially resolved electrochemical video of $Ni_3(HITP)_2$ under an air atmosphere (AVI)

■ AUTHOR INFORMATION

Corresponding Authors

Patrick R. Unwin − *Department of Chemistry, University of Warwick, Coventry CV4 7AL, U.K.;* orcid.org/0000-0003-3106-2178; Email: p.r.unwin@warwick.ac.uk

Mircea Dincă − *Department of Chemistry, Massachusetts Institute of Technology, Cambridge, Massachusetts 02139, United States;* orcid.org/0000-0002-1262-1264; Email: mdinca@mit.edu

Authors

Ruperto G. Mariano − *Department of Chemistry, Massachusetts Institute of Technology, Cambridge, Massachusetts 02139, United States*

Oluwasegun J. Wahab − *Department of Chemistry, University of Warwick, Coventry CV4 7AL, U.K.;* orcid.org/0000-0003-4280-9089

Joshua A. Rabinowitz − *Department of Chemistry, Stanford University, Stanford, California 94305, United States*

Julius Oppenheim − *Department of Chemistry, Massachusetts Institute of Technology, Cambridge, Massachusetts 02139, United States*

Tianyang Chen − *Department of Chemistry, Massachusetts Institute of Technology, Cambridge, Massachusetts 02139, United States;* orcid.org/0000-0003-3142-8176

Complete contact information is available at: https://pubs.acs.org/10.1021/acscentsci.2c00509

Author Contributions

Conceptualization: R.G.M., P.R.U., M.D. Methodology: R.G.M., O.J.W., J.A.R., P.R.U., M.D. Investigation: R.G.M., J.A.R., O.J.W., J.O., T.C. Visualization: R.G.M., J.O., O.J.W. Funding acquisition: R.G.M., P.R.U., M.D. Project administration: R.G.M., P.R.U., M.D. Supervision: P.R.U., M.D. Writing−original draft: R.G.M. Writing−review and editing: R.G.M., O.J.W, J.A.R., J.O., T.C., P.R.U., M.D.

Author Contributions

‖O.J.W. and J.A.R. contributed equally.

Notes

The authors declare no competing financial interest.

■ ACKNOWLEDGMENTS

This work was supported by the National Science Foundation (DMR-2105495), the Research Corporation for Science Advancement (R.G.M., M.D.), the University of Warwick Chancellor's International Scholarship (O.J.W.) and the Royal Society of Chemistry Wolfson Research Merit Award (P.R.U.). The authors are grateful to Prof. Matthew Kanan of Stanford University for access to 3D printing equipment. The authors also thank Dr. Enrico Daviddi, Mr. Joshua J. Tully, and Dr. Gabriel N. Meloni of the University of Warwick for helpful comments and the design and 3D printing of SECCM environmental cells. The SEM imaging performed as part of this work made use of the facilities at MIT.nano. XPS data were collected at the Harvard Center for Nanoscale Systems, a member of the National Nanotechnology Infrastructure Network.

■ REFERENCES

(1) Ren, S.; Joulié, D.; Salvatore, D.; Torbensen, K.; Wang, M.; Robert, M.; Berlinguette, C. P. Molecular Electrocatalysts Can Mediate Fast, Selective CO_2 Reduction in a Flow Cell. *Science.* **2019**, *365* (6451), 367−369.

(2) Xie, L. S.; Skorupskii, G.; Dincă, M. Electrically Conductive Metal-Organic Frameworks. *Chem. Rev.* **2020**, *120* (16), 8536−8580.

(3) *Metal Organic Frameworks for Electrochemical Applications*; Morozan, A., Jaouen, E., Eds.; Royal Society of Chemistry: 2011. DOI: 10.1039/c2ee22989g.

(4) Miner, E. M.; Wang, L.; Dincă, M. Modular O_2 Electroreduction Activity in Triphenylene-Based Metal-Organic Frameworks. *Chem. Sci.* **2018**, *9* (29), 6286−6291.

(5) Miner, E. M.; Gul, S.; Ricke, N. D.; Pastor, E.; Yano, J.; Yachandra, V. K.; Van Voorhis, T.; Dincă, M. Mechanistic Evidence for Ligand-Centered Electrocatalytic Oxygen Reduction with the Conductive MOF Ni_3(Hexaiminotriphenylene)$_2$. *ACS Catal.* **2017**, *7* (11), 7726−7731.

(6) Sheberla, D.; Bachman, J. C.; Elias, J. S.; Sun, C. J.; Shao-Horn, Y.; Dincă, M. Conductive MOF Electrodes for Stable Supercapacitors with High Areal Capacitance. *Nat. Mater.* **2017**, *16* (2), 220−224.

(7) Gu, J.; Hsu, C.-S.; Bai, L.; Chen, H. M.; Hu, X. Atomically Dispersed Fe^{3+} Sites Catalyze Efficient CO_2 Electroreduction to CO. *Science.* **2019**, *364* (6445), 1091−1094.

(8) Wang, H. F.; Chen, L.; Pang, H.; Kaskel, S.; Xu, Q. MOF-Derived Electrocatalysts for Oxygen Reduction, Oxygen Evolution and Hydrogen Evolution Reactions. *Chem. Soc. Rev.* **2020**, *49* (5), 1414−1448.

(9) Kuruvinashetti, K.; Kornienko, N. Linker Modulated Peroxide Electrosynthesis Using Metal-organic Nanosheets. *ChemElectroChem.* **2022**, DOI: 10.1002/celc.202101632.

(10) Majidi, L.; Ahmadiparidari, A.; Shan, N.; Misal, S. N.; Kumar, K.; Huang, Z.; Rastegar, S.; Hemmat, Z.; Zou, X.; Zapol, P.; Cabana, J.; Curtiss, L. A.; Salehi-Khojin, A. 2D Copper Tetrahydroxyquinone Conductive Metal-Organic Framework for Selective CO_2 Electrocatalysis at Low Overpotentials. *Adv. Mater.* **2021**, *33* (10), 2004393.

(11) Sikdar, N.; Junqueira, J. R. C.; Dieckhöfer, S.; Quast, T.; Braun, M.; Song, Y.; Aiyappa, H. B.; Seisel, S.; Weidner, J.; Öhl, D.; Andronescu, C.; Schuhmann, W. A Metal-Organic Framework Derived $Cu_xO_yC_z$ Catalyst for Electrochemical CO_2 Reduction and Impact of Local PH Change. *Angew. Chemie Int. Ed.* **2021**, *60* (43), 23427−23434.
(12) Perfecto-Irigaray, M.; Albo, J.; Beobide, G.; Castillo, O.; Irabien, A.; Pérez-Yáñez, S. Synthesis of Heterometallic Metal-Organic Frameworks and Their Performance as Electrocatalyst for CO_2 Reduction. *RSC Adv.* **2018**, *8* (38), 21092−21099.
(13) Zhang, Q.; Guan, J. Single-Atom Catalysts for Electrocatalytic Applications. *Adv. Funct. Mater.* **2020**, *30* (31), 2000768.
(14) Wang, Y.; Wang, D.; Li, Y. Rational Design of Single-Atom Site Electrocatalysts: From Theoretical Understandings to Practical Applications. *Adv. Mater.* **2021**, *33* (34), 2008151.
(15) Miner, E. M.; Fukushima, T.; Sheberla, D.; Sun, L.; Surendranath, Y.; Dincă, M. Electrochemical Oxygen Reduction Catalysed by Ni_3(Hexaiminotriphenylene)$_2$. *Nat. Commun.* **2016**, *7* (1), 10942.
(16) Lian, Y.; Yang, W.; Zhang, C.; Sun, H.; Deng, Z.; Xu, W.; Song, L.; Ouyang, Z.; Wang, Z.; Guo, J.; Peng, Y. Unpaired 3d Electrons on Atomically Dispersed Cobalt Centres in Coordination Polymers Regulate Both Oxygen Reduction Reaction (ORR) Activity and Selectivity for Use in Zinc-Air Batteries. *Angew. Chemie Int. Ed.* **2020**, *59* (1), 286−294.
(17) Hackley, V. A.; Stefaniak, A. B. Real-World" Precision, Bias, and between-Laboratory Variation for Surface Area Measurement of a Titanium Dioxide Nanomaterial in Powder Form. *J. Nanoparticle Res.* **2013**, *15* (6), 1742.
(18) Zhou, M.; Wei, Z.; Qiao, H.; Zhu, L.; Yang, H.; Xia, T. Particle Size and Pore Structure Characterization of Silver Nanoparticles Prepared by Confined Arc Plasma. *J. Nanomater.* **2009**, *2009*, 1−5.
(19) Sheberla, D.; Sun, L.; Blood-Forsythe, M. A.; Er, S.; Wade, C. R.; Brozek, C. K.; Aspuru-Guzik, A.; Dincă, M. High Electrical Conductivity in Ni_3(2,3,6,7,10,11-Hexaiminotriphenylene)$_2$, a Semiconducting Metal-Organic Graphene Analogue. *J. Am. Chem. Soc.* **2014**, *136* (25), 8859−8862.
(20) Bard, A. J.; Faulkner, L. R. *Electrochemical Methods: Fundamentals and Applications*, 2nd ed.; Wiley: 2000.
(21) Xing, W.; Yin, G.; Zhang, J. *Rotating Electrode Methods and Oxygen Reduction Electrocatalysts*; Elsevier: 2014. DOI: 10.1016/C2012-0-06455-1.
(22) Lide, D. *CRC Handbook of Chemistry and Physics*, 76th ed.; CRC Press: 1996.
(23) Hall, A. S.; Yoon, Y.; Wuttig, A.; Surendranath, Y. Mesostructure-Induced Selectivity in CO_2 Reduction Catalysis. *J. Am. Chem. Soc.* **2015**, *137* (47), 14834−14837.
(24) Yoon, Y.; Hall, A. S.; Surendranath, Y. Tuning of Silver Catalyst Mesostructure Promotes Selective Carbon Dioxide Conversion into Fuels. *Angew. Chem.* **2016**, *128* (49), 15508−15512.
(25) Chen, T.; Dou, J.-H.; Yang, L.; Sun, C.; Libretto, N. J.; Skorupskii, G.; Miller, J. T.; Dincă, M. Continuous Electrical Conductivity Variation in M_3 (Hexaiminotriphenylene)$_2$(M = Co, Ni, Cu) MOF Alloys. *J. Am. Chem. Soc.* **2020**, *142* (28), 12367−12373.
(26) Xing, Z.; Hu, L.; Ripatti, D. S.; Hu, X.; Feng, X. Enhancing Carbon Dioxide Gas-Diffusion Electrolysis by Creating a Hydrophobic Catalyst Microenvironment. *Nat. Commun.* **2021**, *12* (1), 136.
(27) Ripatti, D. S.; Veltman, T. R.; Kanan, M. W. Carbon Monoxide Gas Diffusion Electrolysis That Produces Concentrated C_2 Products with High Single-Pass Conversion. *Joule* **2019**, *3* (1), 240−256.
(28) Mariano, R. G.; Kang, M.; Wahab, O. J.; McPherson, I. J.; Rabinowitz, J. A.; Unwin, P. R.; Kanan, M. W. Microstructural Origin of Locally Enhanced CO_2 Electroreduction Activity on Gold. *Nat. Mater.* **2021**, *20* (7), 1000−1006.
(29) Xing, Z.; Hu, X.; Feng, X. Tuning the Microenvironment in Gas-Diffusion Electrodes Enables High-Rate CO_2 Electrolysis to Formate. *ACS Energy Lett.* **2021**, *6*, 1694−1702.
(30) Xia, C.; Xia, Y.; Zhu, P.; Fan, L.; Wang, H. Direct Electrosynthesis of Pure Aqueous H_2O_2 Solutions up to 20% by Weight Using a Solid Electrolyte. *Science.* **2019**, *366* (6462), 226−231.
(31) Tang, C.; Chen, L.; Li, H.; Li, L.; Jiao, Y.; Zheng, Y.; Xu, H.; Davey, K.; Qiao, S.-Z. Tailoring Acidic Oxygen Reduction Selectivity on Single-Atom Catalysts via Modification of First and Second Coordination Spheres. *J. Am. Chem. Soc.* **2021**, *143* (20), 7819−7827.
(32) Lin, Z.; Zhang, Q.; Pan, J.; Tsounis, C.; Esmailpour, A. A.; Xi, S.; Yang, H. Y.; Han, Z.; Yun, J.; Amal, R.; Lu, X. Atomic Co Decorated Free-Standing Graphene Electrode Assembly for Efficient Hydrogen Peroxide Production in Acid. *Energy Environ. Sci.* **2022**, *15*, 1172.
(33) Wahab, O. J.; Kang, M.; Unwin, P. R. Scanning Electrochemical Cell Microscopy: A Natural Technique for Single Entity Electrochemistry. *Curr. Opin. Electrochem.* **2020**, *22*, 120−128.
(34) Bentley, C. L.; Kang, M.; Unwin, P. R. Nanoscale Surface Structure-Activity in Electrochemistry and Electrocatalysis. *J. Am. Chem. Soc.* **2019**, *141* (6), 2179−2193.
(35) Guo, S.-X.; Bentley, C. L.; Kang, M.; Bond, A. M.; Unwin, P. R.; Zhang, J. Advanced Spatiotemporal Voltammetric Techniques for Kinetic Analysis and Active Site Determination in the Electrochemical Reduction of CO_2. *Acc. Chem. Res.* **2022**, *55* (3), 241−251.
(36) Chen, C.-H.; Meadows, K. E.; Cuharuc, A.; Lai, S. C. S.; Unwin, P. R. High Resolution Mapping of Oxygen Reduction Reaction Kinetics at Polycrystalline Platinum Electrodes. *Phys. Chem. Chem. Phys.* **2014**, *16* (34), 18545−18552.
(37) Bentley, C. L.; Kang, M.; Unwin, P. R. Nanoscale Structure Dynamics within Electrocatalytic Materials. *J. Am. Chem. Soc.* **2017**, *139* (46), 16813−16821.
(38) Mariano, R. G.; McKelvey, K.; White, H. S.; Kanan, M. W. Selective Increase in CO_2 Electroreduction Activity at Grain-Boundary Surface Terminations. *Science.* **2017**, *358* (6367), 1187−1192.
(39) Forster, R. Micro- and Nanoelectrodes. *Encycl. Appl. Electrochem.* **2014**, 1248−1256.
(40) Chen, L.; Kim, J.; Ishizuka, T.; Honsho, Y.; Saeki, A.; Seki, S.; Ihee, H.; Jiang, D. Noncovalently Netted, Photoconductive Sheets with Extremely High Carrier Mobility and Conduction Anisotropy from Triphenylene-Fused Metal Trigon Conjugates. *J. Am. Chem. Soc.* **2009**, *131* (21), 7287−7292.
(41) Wuttig, A.; Surendranath, Y. Impurity Ion Complexation Enhances Carbon Dioxide Reduction Catalysis. *ACS Catal.* **2015**, *5* (7), 4479−4484.
(42) Chen, Z.; Chen, S.; Siahrostami, S.; Chakthranont, P.; Hahn, C.; Nordlund, D.; Dimosthenis, S.; Nørskov, J. K.; Bao, Z.; Jaramillo, T. F. Development of a Reactor with Carbon Catalysts for Modular-Scale, Low-Cost Electrochemical Generation of H_2O_2. *React. Chem. Eng.* **2017**, *2* (2), 239−245.
(43) Yoon, Y.; Yan, B.; Surendranath, Y. Suppressing Ion Transfer Enables Versatile Measurements of Electrochemical Surface Area for Intrinsic Activity Comparisons. *J. Am. Chem. Soc.* **2018**, *140* (7), 2397−2400.
(44) Valavanis, D.; Ciocci, P.; Meloni, G. N.; Morris, P.; Lemineur, J.-F.; Mcpherson, I. J.; Fŕ, F.; Fréd, F.; Kanoufi, F.; Unwin, P. R. Hybrid Scanning Electrochemical Cell Microscopy-Interference Reflection Microscopy (SECCM-IRM): Tracking Phase Formation on Surfaces in Small Volumes. *Faraday Discuss.* **2021**, *233*, 122−148.
(45) Ebejer, N.; Güell, A. G.; Lai, S. C. S.; McKelvey, K.; Snowden, M. E.; Unwin, P. R. Scanning Electrochemical Cell Microscopy: A Versatile Technique for Nanoscale Electrochemistry and Functional Imaging. *Annu. Rev. Anal. Chem.* **2013**, *6* (1), 329−351.
(46) Bentley, C. L.; Kang, M.; Unwin, P. R. Scanning Electrochemical Cell Microscopy: New Perspectives on Electrode Processes in Action. *Curr. Opin. Electrochem.* **2017**, *6* (1), 23−30.
(47) Nam, D.-H.; Shekhah, O.; Lee, G.; Mallick, A.; Jiang, H.; Li, F.; Chen, B.; Wicks, J.; Eddaoudi, M.; Sargent, E. H. Intermediate Binding Control Using Metal-Organic Frameworks Enhances Electrochemical CO_2 Reduction. *J. Am. Chem. Soc.* **2020**, *142*, 21513.
(48) Campbell, M. G.; Sheberla, D.; Liu, S. F.; Swager, T. M.; Dincă, M. Cu_3(Hexaiminotriphenylene)$_2$: An Electrically Conductive 2D

Metal-Organic Framework for Chemiresistive Sensing. *Angew. Chemie Int. Ed.* **2015**, *54* (14), 4349−4352.
(49) Dong, R.; Zheng, Z.; Tranca, D. C.; Zhang, J.; Chandrasekhar, N.; Liu, S.; Zhuang, X.; Seifert, G.; Feng, X. Immobilizing Molecular Metal Dithiolene-Diamine Complexes on 2D Metal-Organic Frameworks for Electrocatalytic H_2 Production. *Chem. - A Eur. J.* **2017**, *23* (10), 2255−2260.
(50) Borysiewicz, M.; Dou, J.; Stassen, I.; Dinca, M. Why Conductivity Is Not Always King - Physical Properties Governing the Capacitance of 2-D Metal-Organic Framework - Based EDLC Supercapacitor Electrodes: $Ni_3(HITP)_2$ as a Case Study. *Faraday Discuss.* **2021**, *231*, 298.
(51) Zhang, G.; Walker, M.; Unwin, P. R. Low-Voltage Voltammetric Electrowetting of Graphite Surfaces by Ion Intercalation/Deintercalation. *Langmuir* **2016**, *32* (30), 7476−7484.

https://doi.org/10.1021/acscentsci.2c00509
ACS Cent. Sci. 2022, 8, 975−982